ACS APPLIED MATERIALS & INTERFACES

Biological and Medical Applications of Materials and Interfaces

Surface Design of Eu-Doped Iron Oxide Nanoparticles for Tuning the Magnetic Relaxivity

Jeong Chan Park, Gyeong Tae Lee, Hee-Kyung Kim, Bokyung Sung, Youngmi Lee, Maengjun Kim, Yongmin Chang, and Jeong Hyun Seo

ACS Appl. Mater. Interfaces, **Just Accepted Manuscript** • DOI: 10.1021/acsami.8b06569 • Publication Date (Web): 10 Jul 2018

ACS Publications

is published by the American Chemical Society. 1155 Sixteenth Street N.W., Washington, DC 20036

Surface Design of Eu-Doped Iron Oxide Nanoparticles for Tuning the Magnetic Relaxivity

Jeong Chan Park,[†] *Gyeong Tae Lee,*[‡] *Hee-Kyung Kim,*[§] *Bokyung Sung,*[∥] *Youngmi Lee,*[⊥] *Maengjun Kim,*[#] *Yongmin Chang,**[△] *, Jeong Hyun Seo,**[‡]

[†]Department of Chemical Engineering
Pohang University of Science and Technology,
77 Cheongam-Ro. Nam-Gu. Pohang. Gyeongbuk. 37673, Korea

[‡]School of Chemical Engineering
Yeungnam University
280 Daehakro, Gyeongsan, Gyeongbuk 38541, Korea
E-mail: jhseo78@yu.ac.kr

[§]Institute of Biomedical Engineering Research
BK21 Plus KNU Biomedical Convergence Program
Kyungpook National University
680 Gukchaebosang-ro, Jung-gu, Daegu 702-701, Korea

[∥] Department of Medical & Biological Engineering
Kyungpook National University
80 Daehakro, Bukgu, Daegu 702-701, Korea

[⊥]Institute of Biomedical Engineering Research
Kyungpook National University
680 Gukchaebosang-ro, Jung-gu, Daegu 702-701, Korea

[#]Korea Multi-purpose Accelerator Complex
Korea Atomic Energy Research Institute
181 Mirae-ro, Geoncheon-eup, Gyeongju, Gyeongbuk, 305-353, Korea

[△]Department of Molecular Medicine
School of Medicine

Kyungpook National University
680 Gukchaebosang-ro, Jung-gu, Daegu 702-701, Korea
E-mail: ychang@knu.ac.kr

KEYWORDS. surface design, relaxivity tuning, hydrophobicity, dual-mode T_1-T_2 MRI nanoprobes, biosensor

ABSTRACT. Relaxivity tuning of nanomaterials with the intrinsic T_1-T_2 dual-contrast ability have great potential for MRI applications. Until now, the relaxivity tuning of T_1 and T_2 dual-modal MRI nanoprobes have been accomplished through the dopant, size, and morphology of the nanoprobes, leaving room for bioapplications. However, a surface engineering method for the relaxivity tuning was seldom reported. Here we report the novel relaxivity tuning method based on the surface engineering of dual-mode T_1-T_2 MRI nanoprobes (DMNP), along with protein interaction monitoring with the DMNP as a potential biosensor application. Core nanoparticles (NPs) of europium-doped iron oxide (EuIO) are prepared by a thermal decomposition method. As surface materials, citrate (Cit), alendronate (Ale), and PMAO/PEG (PP) are employed for the relaxivity tuning of the NPs based on surface engineering, resulting in EuIO-Cit, EuIO-Ale, and EuIO-PP, respectively. The key achievement of the current study is that the surface materials of the DMNP have significant impacts on the r_1 and r_2 relaxivities. The correlation between the hydrophobicity of the surface material and longitudinal relaxivity (r_1) of EuIO NPs presents an exponential decay feature. The r_1 relaxivity of EuIO-Cit is 13.2-fold higher than that of EuIO-PP. EuIO can act as T_1-T_2 dual-modal (EuIO-Cit) or T_2-dominated MRI CAs (EuIO-PP) depending on the surface engineering. The feasibility of using the resulting nanosystem as a sensor for environmental changes, such as albumin interaction, was also explored. The albumin interaction on the DMNP shows both T_1 and T_2 relaxation time changes

as mutually confirmative information. The relaxivity tuning approach based on the surface engineering may provide an insightful strategy for bio-applications of DMNP and give a fresh impetus for the development of novel stimuli-responsive MRI nanoplatforms with T_1 and T_2 dual-modality for various biomedical applications.

INTRODUCTION.

Magnetic resonance imaging (MRI) has become one of the most prominent and widely adapted diagnostic imaging methods in the realm of clinical practice and biomedical research because of its superior spatial resolution and 3D tomographic images with anatomical details. However, MRI has a relatively low sensitivity compared with other imaging methods and the low sensitivity of MRI can be improved with the assistance of contrast agents (CAs).[1-3] MRI CAs enhance the magnetic resonance (MR) signal against the background by altering the spin-lattice relaxation time (T_1) or spin-spin relaxation time (T_2), with the efficiencies usually expressed as the r_1 and r_2 relaxivities, respectively. Longitudinal (T_1) CAs are mainly paramagnetic metal chelates such as Gd-DTPA and Gd-DOTA, which possess a water proton longitudinal relaxivity (r_1) of 3–5 $mM^{-1}s^{-1}$.[4] As reported by our and other groups, nanomaterials such as gadolinium oxide show larger r_1 values than the Gd(III) chelates.[5-6] Although ultrasmall iron oxide (IO) nanomaterials (<4 nm) allow T_1 enhanced images,[7-8] generally, IO-based nanoparticles (NPs) are employed for transverse (T_2) CAs, which have a wide range of water proton transverse relaxivity (r_2) of 30–400 $mM^{-1}s^{-1}$.[9] However, the T_1 signals from MRI CAs can often be confused with endogenous artifacts such as calcification and fat tissues. There is also some difficulty in

differentiating between the T_2 signal from MRI CAs and artifacts that originate from hemorrhages, blood clots, and air.[10]

To settle these issues, T_1-T_2 dual imaging probes, which combine paramagnetic metal ions or complexes and IO-based NPs, have been designed to improve the diagnosis accuracy using orthogonal algorithms.[11-12] Gd(III) ions are of particular interest in constructing DMNP. When used as a dopant, Gd(III) ions exhibit a unique magnetic property, as shown in our previous report,[13] as well as a synergically enhanced MRI performance for T_1-T_2 dual imaging.[14] Europium (Eu) (III) ions are also used in the design of DMNP.[15]

To date, the realization and relaxivity tuning of MRI nanoprobes have been attained through the dopant, size, and morphology of nanomaterials,[16-18] providing opportunities for sensing applications of DMNP.[12] Recently, magnetic resonance tuning based on T_1 and T_2 materials, called distance-dependent magnetic resonance tuning (MRET), has been demonstrated as a method to investigate diverse biological systems.[19] MRET is a novel sensing principle that uses superparamagnetic NPs and gadolinium (Gd) complexes as the quencher and enhancer, respectively. The positive T_1 MRI intensity is tuned based on the separation distance between the superparamagnetic NP quencher and the paramagnetic T_1 enhancer.

Thus, the relaxivity tuning concept based on the combination of T_1 and T_2 materials is still in demand and in the early stage. In addition, the impacts of surface engineering on the magnetic relaxation property have mostly been studied with IO or Gd-based nanocrystals.[20-23] IO NPs coated with PF 127 co-polymers exhibited a high r_2/r_1 ratio due to the segregation from the external water molecules by the hydrophobic surface layer.[20] $NaGdF_4$ nanocrystal-micelles showed the high r_1 relaxivity by controlling the surface structure of the nanocrystals.[23] The strategy for the enhancement of $NaGdF_4$ relaxivity was demonstrated by using surface ligands

having strong interaction with water molecules.[22] Herein, we report the relaxivity tuning of DMNP through surface engineering. In addition, we report that both the T_1 and T_2 relaxation times of DMNP change upon protein interaction with the NPs, which provide mutually confirmative logic to enhance the determination accuracy.

EXPERIMENTAL SECTION

Materials. Europium (III) acetate hydrate, amino PEG, Vivaspin 6, and syringe filters (PTFE, 0.1 μm) were purchased from Alfa Aesar, Nanocs, Sartorius, and Whatman, respectively. Oleic acid (OA), oleylamine (OM), and alendronate sodium trihydrate were obtained from TCI chemicals. All other chemicals and reagents were purchased from Sigma-Aldrich and used as received.

Fabrication of EuIO. EuIO was synthesized by a thermal decomposition method.[24] Briefly, Eu (III) acetate (0.1 mmol) was added to benzyl ether (20 mL). The solution was heated to 100°C and stirred for 40 min under a nitrogen atmosphere. 1 mmol of $Fe(acac)_3$ as iron precursors, 3 mmol of oleylamine, 3 mmol of oleic acid and 5 mmol of 1,2 hexadecanediol were added to the above solution. The mixture was heated to 200°C and maintained for 1 h. The solution was then heated to 270°C and reacted for 1 h. After cooling at room temperature, ethanol (40 mL) was added to the reaction mixture and centrifuged to obtain the resulting products, which were redispersed in 20 mL of hexane.

Preparation of EuIO-Cit, -Ale, and -PP. (i) EuIO-Cit; Sodium citrate (100 mg) was dissolved in 8 mL of distilled water and mixed with 8 mL of EuIO dispersed in hexane, according to the modified procedures.[25] Acetone (12 mL) was added to the above mixture and stirred at 65°C for 4 h. After reaction, the solution was centrifuged using Vivaspin 6 (MWCO 10,000) spin concentrators. This centrifugation step was repeated thrice.

(ii) EuIO-Ale; A EuIO hexane solution (2 mL) and tetrahydrofuran (THF, 2 mL) mixture was added to an alendronate sodium trihydrate (50 mg) aqueous solution at pH 9, which was adjusted using a NaOH solution as previously described.[26] The reaction solution was stirred for 2 d, and the products were collected by applying a magnet. The collected products were redispersed in distilled water.

(iii) EuIO-PP; Amino-functionalized poly(-ethylene glycol) methyl ether (mPEG-NH_2) and Poly(maleic anhydride-alt-1-octadecene) (PMAO) (mPEG-NH_2:PMAO molar ratio = 30:1) were mixed in chloroform, according to the previous procedure.[27-28] The EuIO NPs in chloroform (5 mL) were added drop wise to the PMAO/PEG mixture (5 mL) and stirred overnight at room temperature. After the reaction, distilled water (10 mL) was added to the reaction solution, and evaporated to remove the chloroform. After evaporation, chloroform (5 mL) was added to the aqueous media, and then the solution was shaken. The mixture was left at room temperature for the layer separation. After the separation, the aqueous layer was collected and heated to 70°C for 30 min to remove the remaining solvents. All of the final products (EuIO-Cit, EuIO-Ale, and EuIO-PP) were passed through a 0.1 μm filter before the experiment.

Contact angle measurement. A cylindrical mold having 10 mm in diameter and 35 mm in height was used to prepare pellets of the surface materials (citrate, alendronate and PMAO). Each of the materials (0.5 g) was used to fill the mold and compressed at 120 MPa using a manual hydraulic press (J-1, Asone, Osaka, Japan) to obtain pellets. The contact angle of the pellets was measured using a SmartDrop (Femtobiomed, Inc., Korea).

Colloidal stability study. EuIO NPs (EuIO-Cit, -Ale, and -PP) were dissolved in various pH solutions (pH value varied from 2 to 10) and evaluated by visual observation for 6 days at room temperature. The pH solutions were prepared with adding 0.1 N HCl or 0.1 N NaOH solutions.

Characterization. The morphologies of the prepared NPs were observed using transmission electron microscopy (TEM, H-7600 microscope, Hitachi, Japan), and the element mapping of the NPs was examined with TEM (JEM-2200FS, JEOL Co., Japan). X-ray diffraction (XRD, X'pert pro, Philips) analysis was performed by using a Cu Kα X-ray source (λ=1.54056 Å) to explore the crystalline structure of the NPs. To verify the presence of Eu ions, X-ray photoelectron spectroscopy (XPS) instrument equipped with a monochromatic Al Kα X-ray source (15,000 eV, 150 W) was utilized. The magnetization curves of the resulting NPs were acquired by using a Quantum Design MPMS XL-7. To determine the element (Eu and Fe ions) concentration, inductively coupled plasma optical emission spectrometry (ICP-OES, Optima 8300 PerkinElmer) was carried out. The hydrodynamic diameter of the NPs was characterized using a dynamic light scattering analysis (Nano ZS, Malvern Instruments, Malvern, UK). Thermal gravimetric analysis (TGA) was performed on a thermogravimetric analyzer (Q500, TA instruments, USA) from 25°C to 600°C at a heating rate of 10°C/min.

Cell viability assay. Mouse liver cell line NCTC 1469 was split into a 96-well plate ((1×10^4 cells/well)/200 μL). As the cell culture medium, Dulbecco's modified Eagle medium (DMEM, Gibco) was used with heat-inactivated horse serum (10%), penicillin (100 IU/mL), and streptomycin (100 mg/mL) and the culture medium was changed to fresh medium every 2 days. Solutions of EuIO-Cit, EuIO-Ale, and EuIO-PP (0.5−50 μM) were respectively added to the serum-free medium and incubated for 24 h. Then, cell viability was measured with CCK-8 kit (10 μL). After removing solution, the absorbance at 450 nm was measured using a microplate reader (Biorad 550 reader, Molecular Devices, Sunnyvale, CA, USA) to estimate the cell viability.

Relaxivity. T_1 measurements were performed at 1.5 T MR scanner (GE Healthcare, Milwaukee, WI, USA) using an inversion recovery (IR) pulse sequence. The IR images were acquired at 35 different inversion times ranging from 50 to 1750 ms. T_1 relaxation rate was estimated using the nonlinear least-squares regression of the signal intensity measured at each inversion time. Carr−Purcell−Meiboom−Gill (CPMG) pulse sequence was employed for T_2 measurements. The images were acquired at 34 different echo times (TEs) ranging from 10 to 1900 ms. T_2 relaxation rate was estimated using the nonlinear least-squares fit of the signal intensity measured at each echo time. Finally, the T_1 and T_2 relaxivities were estimated using the linear fit of each relaxation rate with 5 different concentrations (1, 0.5, 0.25, 0.125, and 0.0625 mM). To measure the ΔR_i of EuIO upon the BSA addition, a EuIO-Cit aqueous solution (100 μL) was mixed with the BSA solutions (30, 3, 0.3, 0.03, and 0.003 μM) and filled up with distilled water to make a final reaction volume of 500 μL.

In vivo MRI experiments. All MR experiments using animals were performed in accordance with the regulations of the Animal Internal Review Board of Kyungpook National University. For in vivo MRI, male ICR mice (average weights of 30 g) were utilized. Isoflurane (1.5%) in oxygen was used to anesthetize the mice. After tail vein injection of EuIO-Cit, the MR images were acquired up to 24 hours at a 1.5 T MR scanner. The injection dose was 2 mg/kg. The animals were kept at ~ 37 °C using a blanket during MRI acquisition. A homemade birdcage-shaped rf coil of the receiver only type (inner diameter of 50 mm) was used for in vivo MR images. The imaging parameters of the T_1 SE measurements were: repetition time (TR) = 300 ms; echo time (TE) = 11 ms; field of view (FOV) = 8 mm; matrix size = 192 × 128; slice thickness = 2.0 mm; number of averaging (NEX) = 8; total scan time = 3 min 16 s. In case of T_2 images the parameters were: TR = 2000 ms; TE = 40 ms; FOV = 8 mm; matrix size = 256 × 192; slice

thickness = 2.0 mm; NEX = 8; total scan time = 2 min 44 s. For semi-quantitative analysis, the signal intensities were measured at several regions of interests (ROIs) and contrast-to-noise ratio (CNR) was calculated up to 24 hours post injection using Equation (1), where SNR is the signal-to-noise ratio.

$$CNR = SNR_{post} - SNR_{pre} \quad (1)$$

RESULTS AND DISCUSSION

Synthesis and Characterization of EuIO. Figure 1 shows that the intrinsic dual-contrast ability of EuIO NPs is tunable through surface engineering. The surfaces of EuIO NPs were engineered for tuning the MRI relaxivity, giving rise to the different r_2/r_1 ratios, by using three different materials: citrate (Cit), alendronate (Ale), and PMAO/PEG (PP) (Figure S1). PP coating would give rather bulk shells to the NPs, compared to the small molecules (Cit and Ale). The hydrophilic nature PEG endows the NPs with water solubility and allows doing application research of the NPs in aqueous media.[29-31] Basically, EuIO NPs have a T_1-T_2 dual-modal MRI contrast ability as a result of the lanthanide and IO materials.

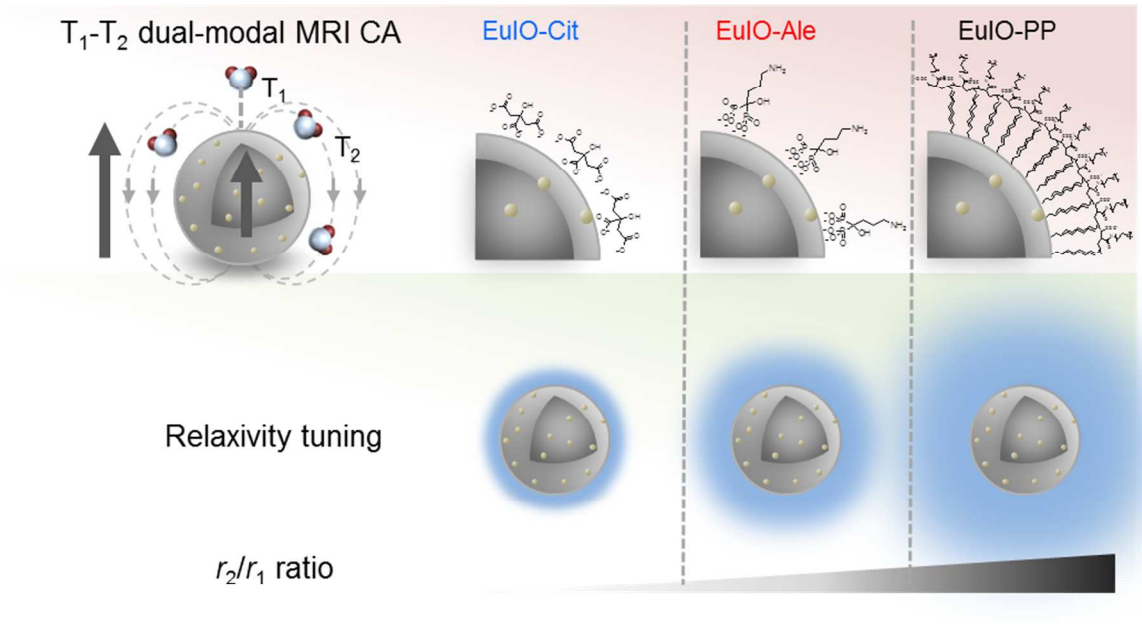

Figure 1. Schematic illustration of relaxivity tuning of MRI nanoprobes with T_1-T_2 dual-modality through surface engineering.

A transmission electron microscopy (TEM) analysis showed 4.9 ± 1.1 nm EuIO NPs, which were prepared in an organic phase using a thermal decomposition method (Figure 2a and b). Our EuIO NPs were smaller than the previous reported EuIO nanocubes.[15] The magnetic properties, shape and size of the ferrite nanomaterials are considerably affected by the synthesis routes.[32-34] Figure 2c presents the XRD patterns of EuIO, showing that all of its peak positions match well with the magnetic NPs (ICSD card no. 98-009-8087). It clearly reveals that EuIO NPs have the cubic spinel structure. We observed no apparent crystal structural alteration upon Eu-doping into the parent magnetite NPs, which was consistent with a previous observation.[32, 35] The X-ray photoelectron spectra (XPS) of EuIO verified the doping of Eu ions (Figure 2d–f). The peaks were fitted by employing the mixed Gaussian-Lorentzian functions and the background was removed by using a Shirley-type shape. The XPS spectra of the carbon and oxygen peaks

implied the presence of organic surfactants such as oleic acids and oleylamines with the NPs. The peaks at 710.3 and 724.9 eV were assigned to $Fe2p_{3/2}$ and $Fe2p_{1/2}$, respectively. The binding energy of $Eu3d_{5/2}$ (1135.3 eV) was assigned to Eu_2O_3, which indicates Eu ions exists in the form of +3 oxidation states in the parent NPs.[32] The area ratio of Eu3d and Fe2p peak was approximately 20%, indicating that the NPs included Eu ions. As shown in Figure 2g–i, an electron energy-loss spectrum (EELS) mapping analysis also confirmed that the EuIO NPs included Eu ions and Fe ions. The Eu doping level was confirmed by using elemental analysis of TEM and ICP-OES (Table S1). EuIO NPs showed superparamagnetic behavior at room temperature (Figure S2). The field-dependent magnetization (M-H) curve indicate that the estimated saturation magnetization of EuIO NPs (~ 42 emu/g) is lower than that (~ 60 emu/g) of IO NPs with similar size in diameter.[36] The doping of Eu ions with low magnetic moment may decrease the saturation magnetization of EuIO NPs.[15, 37]

The TEM images in Figure 3 show that EuIO NPs were transferred into water using Cit, Ale, and PP, maintaining the morphology and size of the EuIO NPs in the organic phase, and were well dispersed in water. We observed rather aggregated EuIO-Ale in TEM images compared to EuIO-Cit and -PP (Figure 3 and Figure S3). We employed two different approaches for the surface engineering, as shown in the scheme of Figure 3. One was the ligand exchange method for EuIO-Cit[25] and -Ale,[26] and the other was the encapsulation structure using amphiphilic polymers for EuIO-PP.[27] Dynamic light scattering (DLS) measurements of the surface-coated EuIO NPs were performed after syringe filtration (0.1-μm pore) (Figure S4). The EuIO NPs (EuIO-Cit, -Ale, and -PP) had good colloidal stability at various pH ranges (Figure S5). The NPs solutions were optically clear without aggregations over a wide range of pH values (pH 2~10).

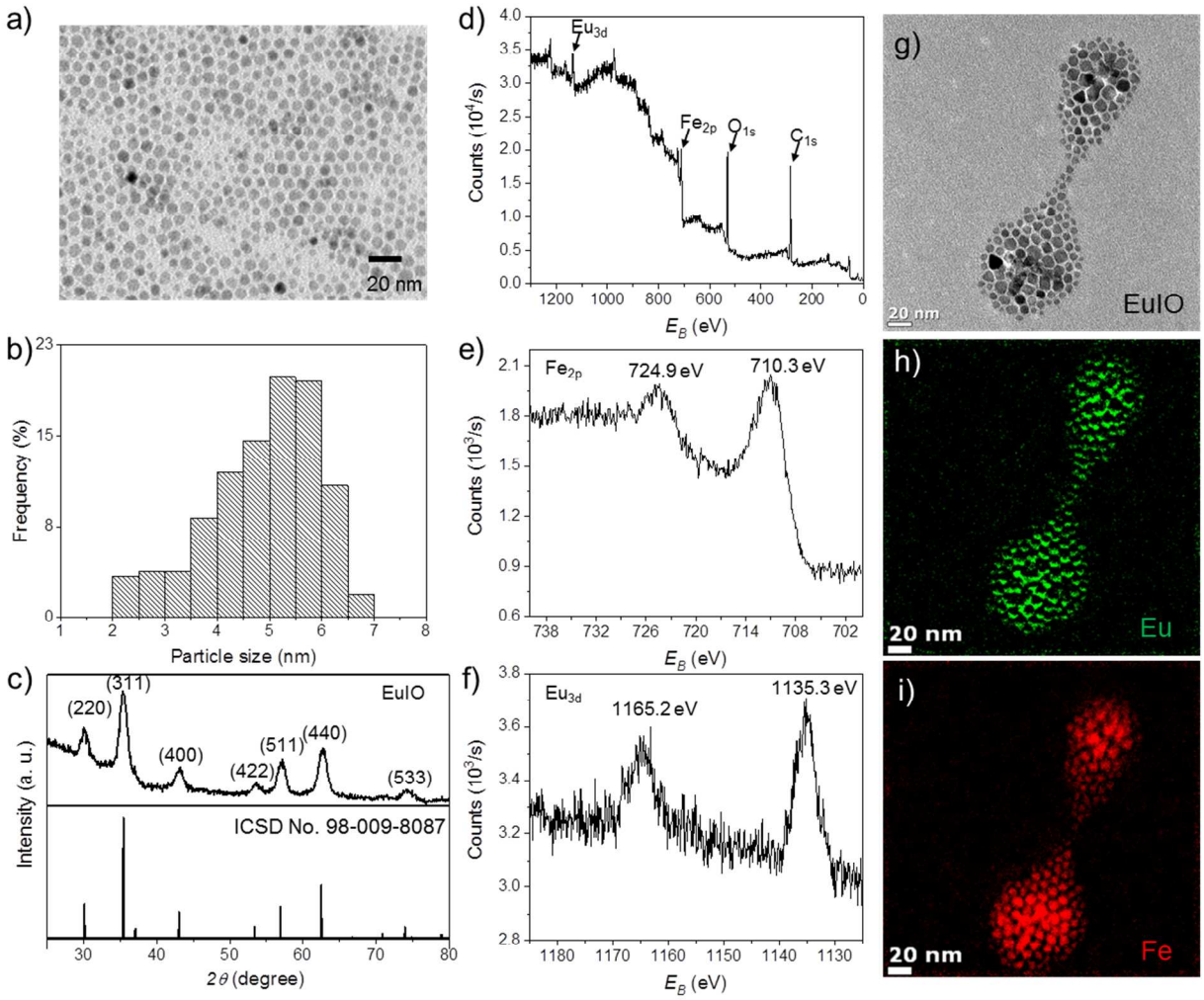

Figure 2. Characterization of EuIO NPs: a) TEM image, b) corresponding size distribution, c) X-ray diffraction pattern, and d) X-ray photoelectron spectroscopy (XPS) images of EuIO NPs. High-resolution XPS spectra of e) Fe region and f) Eu region of EuIO NPs. g–i) Element mapping analysis of EuIO NPs: g) TEM image, h) Eu mapped image, and i) Fe mapped image of EuIO.

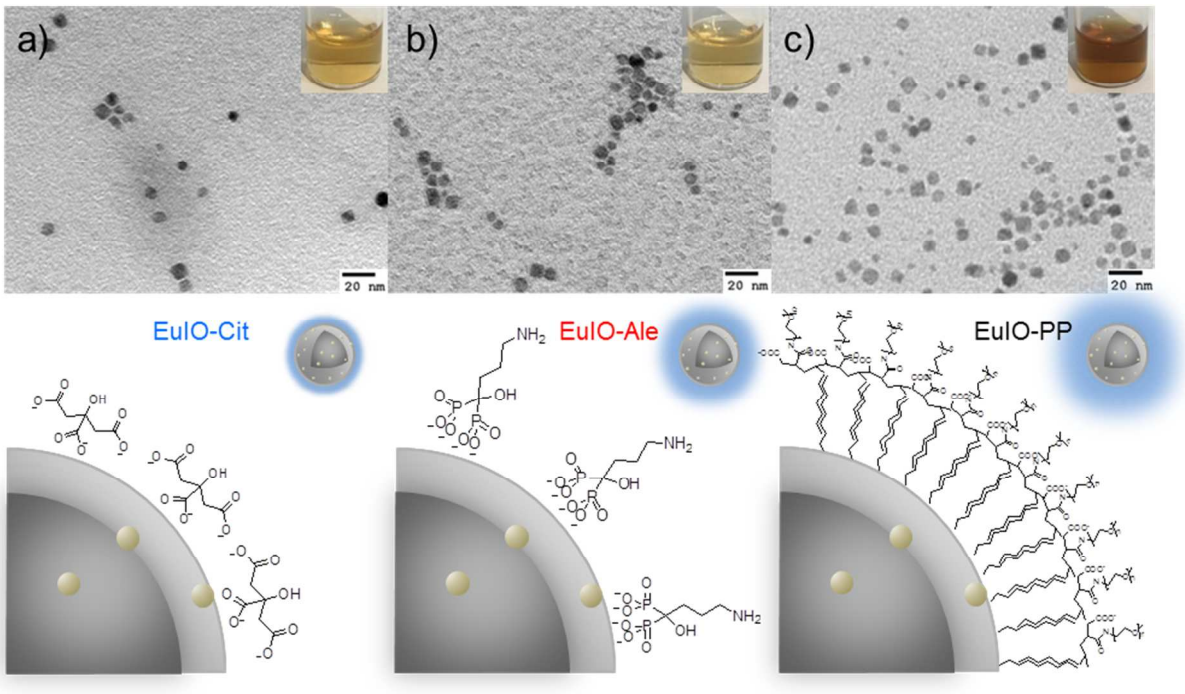

Figure 3. TEM images of EuIO coated with a) citrate (Cit), b) alendronate (Ale), and c) PMAO-PEG (PP). Schematic illustrations of surface engineering of EuIO with Cit, Ale, and PP are shown below the corresponding TEM images.

MRI Enhancement Performance and Relaxivity Measurement. The MRI contrast enhancement performance of the EuIO NPs in relation to the surface engineering was investigated using a 1.5 T MRI scanner. T_1 and T_2 images of EuIO-Cit, -Ale, and -PP are shown in Figure 4a. EuIO-Cit shows a strong T_1 enhancement, and EuIO-PP presents a weak T_1 contrast, indicating that the order of the T_1 effect is EuIO-Cit > EuIO-Ale > EuIO-PP. Interestingly, EuIO-Ale reveals a stronger T_2 effect than EuIO-Cit and EuIO-PP. Surface engineering of magnetic nanomaterials would tune the T_1 or T_2 effect, as previously reported.[21-22] To further examine the

surface-based relaxivity tuning of DMNP, the r_1 and r_2 relaxivities of EuIO NPs were measured (Figure 4b and c).

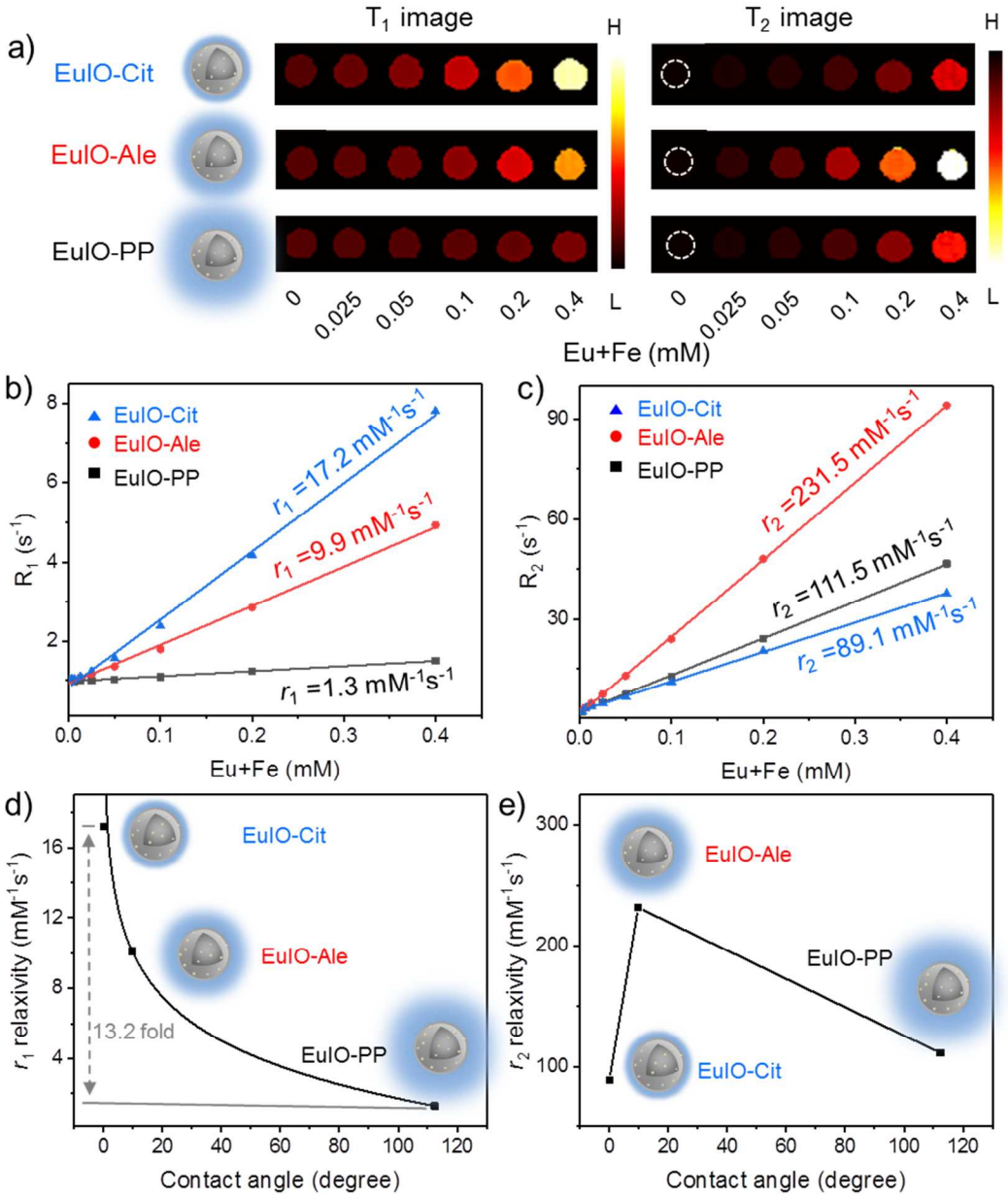

Figure 4. a) T_1 and T_2 images of EuIO-Cit, -Ale, and -PP as function of Eu (III) and Fe (III) ion concentrations. b) r_1 and c) r_2 relaxivity values of EuIO-Cit, -Ale, and -PP. Plots of d) r_1 and e) r_2 relaxivities as a function of contact angle.

EuIO-Cit showed an r_1 value of 17.2 $mM^{-1}s^{-1}$ and r_2 value of 89.1 $mM^{-1}s^{-1}$. The r_1 and r_2 values of EuIO-Cit (~5 nm) were comparable to those (r_1 = 36.8 $mM^{-1}s^{-1}$ and r_2 = 97.5 $mM^{-1}s^{-1}$) of the EuIO NPs reported in Table S2, considering the larger size (14 nm) of the reported NPs and the increase in r_1 and r_2 with an increase in the NPs core size according to the outer sphere theory.[15] EuIO-Cit provides a larger r_1 than Gd(III)-chelates such as Gd-DTPA, as listed in Table S2, which is probably originate in the cooperative induction effect of the surface Eu ions in EuIO-Cit.[5] Citrate, which is a small molecule and a highly hydrophilic material, allows the highly water permeable environment around the NPs surface. Carboxylic groups in citrate may also contribute to the higher r_1 relaxivity of EuIO-Cit.[22] The ratio of r_2/r_1 is the critical factor to estimate the T_1 or T_2 contrast efficacy of the given MRI CAs. The material with a relatively high r_2/r_1 ratio (>8) is the T_2-dominated MRI CAs,[18] whereas a moderate r_2/r_1 ratio gives rise to MRI probes with T_1-T_2 dual-modality.[17] When the r_2/r_1 ratio is close to one, a material is a good candidate for T_1 CAs.[38] The r_2/r_1 ratio of EuIO-Cit was 5.2, which allowed it to act as DMNP, as shown in Figure 4. The higher r_1 relaxivity of EuIO-Cit compared to EuIO-Ale and -PP would be attributed to the small and hydrophilic surface coating, which endowed the surface of the core NPs with a highly water-permeable environment and increased the accessibility of the surrounding water molecules to the Eu ions on the surface of the EuIO NPs.

The controlling the access of the water molecules to the magnetic cores is one of the critical parameters to tune the r_1 relaxivity of MRI CAs.[5, 39-40] The hydrophobicity of surface materials of NPs would affect the water molecules access to the magnetic cores. Thus, we explored the hydrophobicity of the materials (Cit, Ale, and PMAO) by measuring the contact angle, as shown in Figure S6, which is generally used to evaluate the hydrophobicity. In the case of Cit, water spread out completely on the Cit surface. Thus, the contact angle was immeasurable. The contact

angles of Ale and PMAO were 9.8° and 112.4°, respectively, indicating that the hydrophobicity order was Cit < Ale <<PMAO. The order of the r_1 relaxivity for the EuIO NPs was EuIO-Cit > EuIO-Ale >> EuIO-PP.

EuIO-PP had an r_2 value of 111.5 $mM^{-1}s^{-1}$ and r_1 value of 1.3 $mM^{-1}s^{-1}$. These results showed that EuIO-PP (r_2/r_1 ratio = 85.8) was a T_2-dominated MRI contrast agent like POA@SPION, as listed in Table S2, which has a similar shell formation (hydrophobic bi-layers and a long PEG chain) leading to a higher r_2/r_1 ratio by reducing the T_1 contrast effects.[20] The r_1 relaxivity of EuIO-PP was significantly decreased compared with the r_1 of EuIO-Cit. The surface modification of NPs would significantly influence on the T_1 relaxation enhancement as demonstrated in $NaGdF_4$ nanocrystals (Table S2).[23] The lower r_1 of EuIO-PP originated in the hydrophobic bi-layers and the long length of the PEG chain of PP surface materials. The hydrophobic octadecene tail of PMAO could interact with the hydrophobic alkane chains of oleic acid (OA)/oleylamine (OM) on the surface of the core NPs to form a bi-layer of the long hydrophobic chains of OA/OM-octadecene. The hydrophobic bi-layers disturbed the water molecule access, giving rise to the reduced r_1 values. The hydrophilic PEG tails imparted water solubility to the EuIO NPs. However, the long chains of PEG (Mw of ~5,000) in EuIO-PP would also contribute to the reduction of the r_1 relaxivity, because an increase in the length of the PEG chains decreased the r_1 values.[41]

In the case of EuIO-Ale, the r_2 and r_1 values were 231.5 $mM^{-1}s^{-1}$ and 9.9 $mM^{-1}s^{-1}$, respectively. The higher r_2 values of EuIO-Ale compared with that of EuIO-Cit may have come from the NPs aggregation and the phosphate group in alendronate. The carboxylate groups in the citrate caused spin canting in the surface layer, which reduced the saturation magnetization, whereas no surface canting effects occurred and the magnetization was preserved in the

phosphate case.[42] The transverse (r_2) relaxivity of the NPs was proportional to the magnetization. This may have caused the higher r_2 relaxivity of EuIO-Ale compared to that of EuIO-Cit. The decreased r_1 value of EuIO-Ale compared with that of EuIO-Cit would be attributed to the more hydrophobic alendronate compared to that of citrate (Figure S1), which disturbed the water molecule access. The order of the r_1 relaxivity for the EuIO NPs was EuIO-Cit > EuIO-Ale >> EuIO-PP. This trend showed a certain relationship between the r_1 relaxivity and the hydrophobicity of the surface materials of the EuIO NPs; the order of hydrophobicity was Cit < Ale << PMAO. A higher hydrophobicity would reduce the water molecule accessibility and lead to a decrease in the r_1 relaxivity. As shown in Figure 4d and e, the relationship between the hydrophobicity and r_1 relaxivity of EuIO NPs shows an exponential decay characteristic, whereas there is no noticeable dependence between the r_2 relaxivity of EuIO and the hydrophobicity of the surface materials of the NPs. The r_1 relaxivity of EuIO-Cit was 13.2-fold higher than that of EuIO-PP. Our observation indicates that the hydrophobicity of the surface materials would be one of the key parameters in designing DMNP.

Cell Viability and In Vivo MRI Performance. We investigated the cytotoxicities of EuIO-Cit, -Ale, and -PP using a CCK-8 assay. An in vitro cytotoxicity test showed the good biocompatibility of the resulting EuIO NPs (Figure S7). We estimated the in vivo MRI enhancement performance of EuIO-Cit using ICR mice. Before and after the intravenous administration of EuIO-Cit (2 mg (Eu+Fe)/kg of animal body weight), T_1-weighted MR images were acquired using a 1.5 T MR scanner. T_1-weighted MR images were obtained up to 24 hours after injection. As shown in Figure 5a, a bright MR signal was observed in organs such as heart, liver and kidney at early time point after the injection and then the MR signal became dark as EuIO-Cit left the organ at late time points. The corresponding T_1 contrast-to-noise ratio (CNR)

values in the various organs showed an increase in the signal intensity up to 20 min and then gradually decreased up to 24 hours after injection (Figure 5b). Among organs, the heart showed highest T_1 CNR increase and the liver showed lowest T_1 CNR increase. It is interesting to note that the liver showed strong decrease in T_1 CNR after initial increase at early time point. Because nano-sized materials with a hydrodynamic diameter larger than 5 nm are generally highly accumulated in the liver by the immune defense, including the mononuclear phagocyte system (MPS),[43] EuIO-Cit was gradually accumulated in the liver after injection and the high concentration of paramagnetic EuIO-Cit in the liver seems to give stronger T_2 effect than T_1 effect. Therefore, the liver showed lower T_1 CNR than pre-contrast T_1 CNR at the late time points.

T_1-weighted MR images and the corresponding T_1 CNR curves up to 24 hours provide qualitative information on the in vivo biodistribution of the EuIO-Cit. First, the signal intensity of heart maintained a high value until 30 minutes and then slowly returned to pre-contrast value until 24 hours suggesting that EuIO-Cit removed from the heart within 24 hours. Therefore, when combining with observation that the animal showed normal behaviour after MRI measurement, the heart toxicity of EuIO-Cit seems to be minimal. Second, the signal intensity of kidney and bladder also showed initial high values and then decreased at late time points suggesting that a small amount of EuIO-Cit might be removed from kidney in vivo. Third, as mentioned, the strong decrease of the signal intensity in liver showed that EuIO-Cit was accumulated in the liver. Finally, the abdominal artery showed bright signal up to 3 hours suggesting that EuIO-Cit was circulating in vasculature relatively long times. However, the quantitative in vivo biodistribution study of the EuIO-Cit using inductively coupled plasma (ICP) spectrophotometer will be warranted in the future.

We also examined the T_2 signal enhancement at the various organs using the T_2-weighted MR images over time (Figure 6a). Among organs, the liver and the abdominal artery showed dark signal from the early time point due to T_2 effect of EuIO-Cit. As shown in Figure 6b, the T_2 CNRs in the other organs showed initial increase in CNR and then showed decrease indicating that our nanosystem works well for an in vivo system.

Figure 7 showed the possible application of EuIO-Cit as DMNP. For the same organ (liver), the T_1-weighted and T_2-weighted MR images showed dual-contrast enhancement at the early time points. That is, at 5 minutes after injection of EuIO-Cit, the T_1-weighted images (Figure 7a) showed bright signal enhancement in the liver with T_1 effect of EuIO-Cit and the T_2-weighted images (Figure 7b) showed dark signal enhancement in the liver with T_2 effect of EuIO-Cit. As mentioned above, due to accumulation of EuIO-Cit in liver, the liver enhancement became dark in T_1-weighted MR images at the late time points.

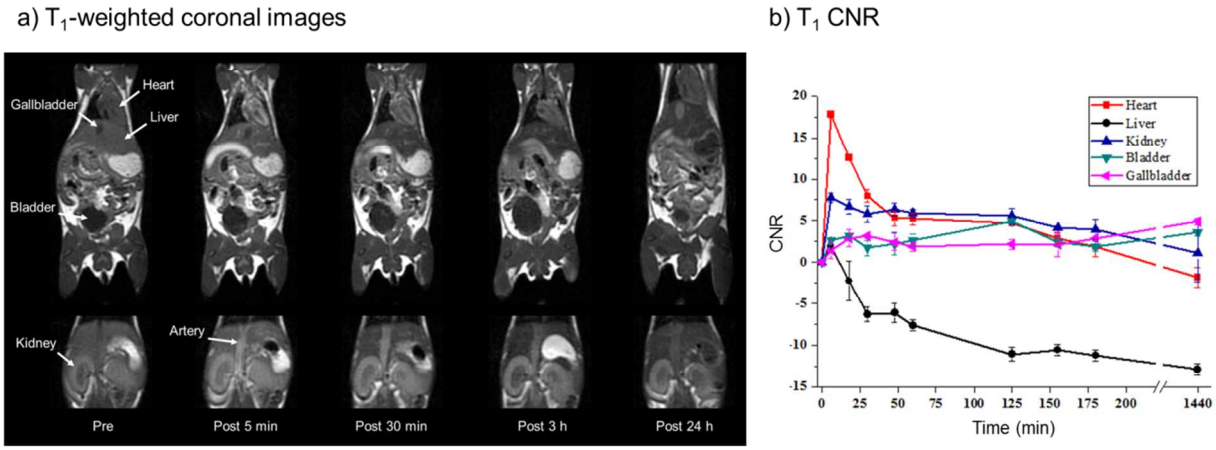

Figure 5. In vivo T_1-weighted coronal images of animal model and MR signal changes in various regions of interest. a) T_1-weighted MR images of mice before and after intravenous

administration of EuIO-Cit up to 24 hours after injection. The arrows indicate the regions of the various organs. b) Contrast-to-noise ratio measurement of the regions of the various organs in T_1-weighted MR images over times up to 24 hours.

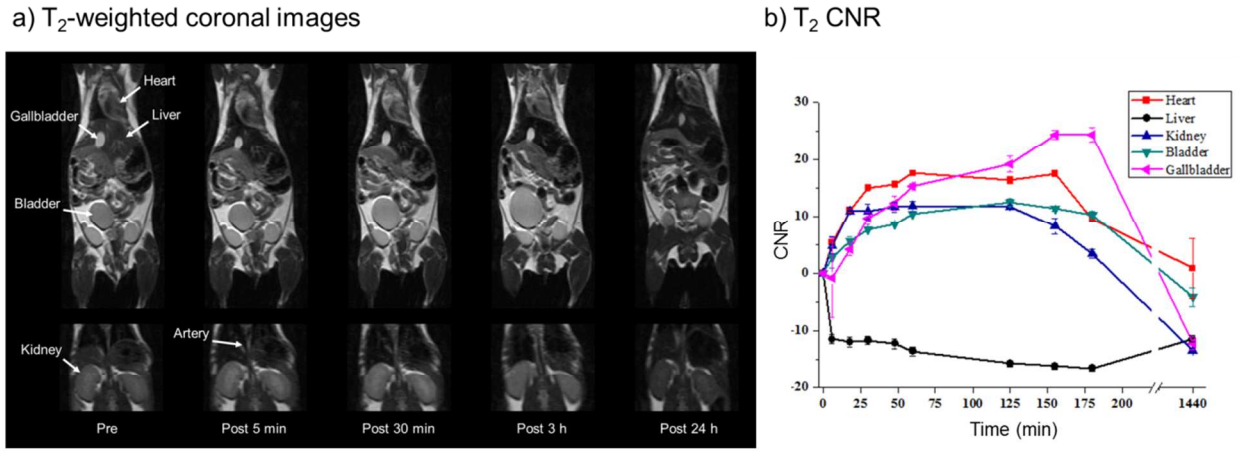

Figure 6. In vivo T_2-weighted coronal images of animal model and MR signal changes in various regions of interest. a) T_2-weighted MR images of mice before and after intravenous administration of EuIO-Cit up to 24 hours after injection. The arrows indicate the regions of the various organs. b) Contrast-to-noise ratio measurement of the regions of the various organs in T_2-weighted MR images over times up to 24 hours.

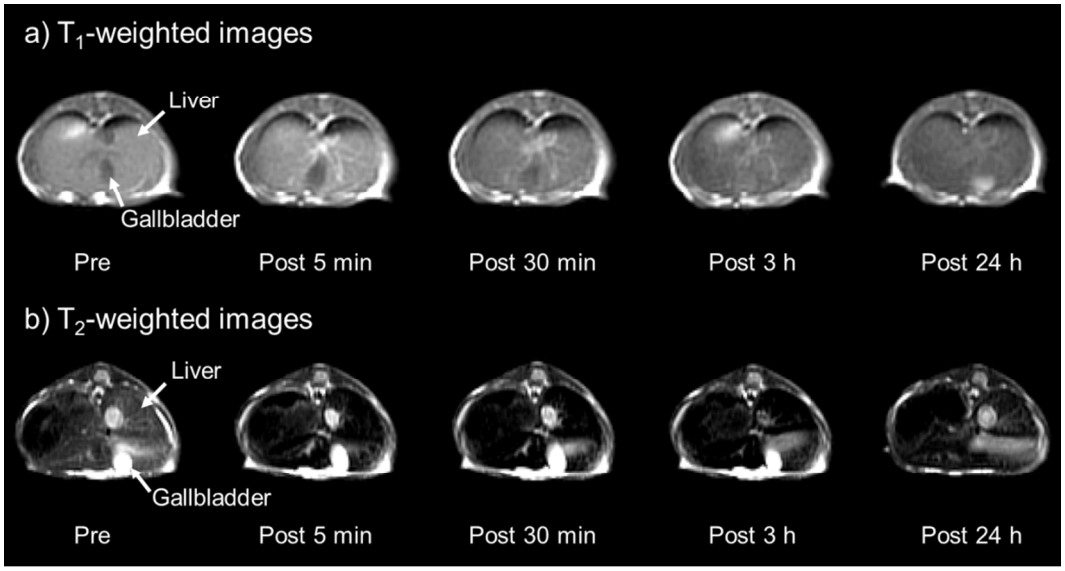

Figure 7. T_1- and T_2-weighted MR images for liver showed dual-contrast enhancement at the early time points. After injection, a) the T_1-weighted images showed bright signal enhancement in the liver with T_1 effect of EuIO-Cit and b) the T_2-weighted images showed dark signal enhancement in the liver with T_2 effect of EuIO-Cit.

Monitoring Protein Interactions. To examine a possible sensing application based on the relaxivity tuning strategy of MRI nanoprobes with T_1-T_2 dual-contrast ability for monitoring environmental changes such as protein interactions, ΔR_i of EuIO-Cit, which was defined as the relaxation time difference ($R_i = 1/T_i$, i = 1 or 2) for $R_{i(NPs+BSA)}$-$R_{i(NPs)}$, was measured upon the addition of bovine serum albumin (BSA) (Figure 8).

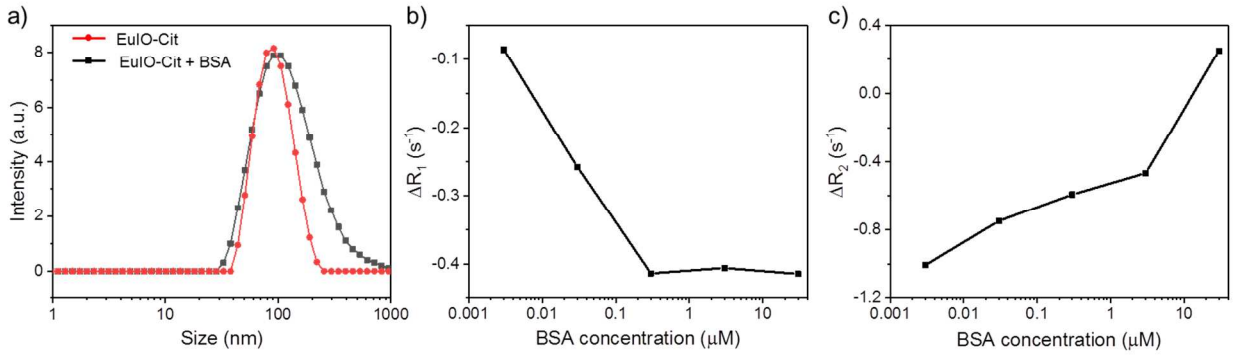

Figure 8. Interaction of EuIO-Cit and BSA. a) Hydrodynamic size of EuIO-Cit before and after BSA incubation. Plots of the differences in b) R_1 and c) R_2 as a function of the BSA concentrations.

DLS measurements revealed that the average hydrodynamic diameters of the NPs increased 143 nm upon the BSA addition (Figure 8a). TGA curves also demonstrated the binding of BSA with EuIO-Cit (Figure S8). The larger mass loss around 100°C would be due to residual water evaporation.[44] Starting from 190°C to 600°C, the major loss of BSA and citrate occurred.[44-45] BSA could bind with citrate, mainly as a result of electrostatic interactions.[46] As the BSA concentration increased in the EuIO-Cit solution, ΔR_1 of EuIO-Cit showed negative values. At a high BSA concentration (>0.03 μM), ΔR_1 of EuIO-Cit exhibited saturated stages (Figure 8b). The negative ΔR1 values for EuIO-Cit upon the BSA addition could be ascribed to the water accessibility to NPs. In other words, as the BSA concentration increased, more BSA interacted with the EuIO-Cit NPs, and thus the accessibility of bulk water to EuIO-Cit became difficult. Because R_1 is dependent on the water accessibility to the surrounding NPs, ΔR_1 of EuIO-Cit decreased as more BSA interacted with the EuIO-Cit NPs. On the other hand, interestingly, ΔR_2 of EuIO-Cit showed an increasing trend as the BSA concentration increased (Figure 8c). The increasing trend for ΔR_2 of EuIO-Cit upon the BSA addition could be explained by the fact that the proteins, including BSA, often showed diamagnetic behaviors.[47] Because the diamagnetism of BSA could partially cancel the superparamagnetism of EuIO-Cit (total magnetization = (EuIO-Cit)superparamagnetic – (BSA)diamagnetic), the R_2 of EuIO-Cit, which was dependent on the superparamagnetism of EuIO-Cit, increased as more BSA interacted with the EuIO-Cit. Finally, the BSA interaction data suggested that the EuIO-Cit could report on the BSA

interaction based on mutually confirmative information, coming from the changes of the T_1 and T_2 relaxation of EuIO-Cit.

CONCLUSIONS

We presented a novel strategy for the relaxivity tuning of DMNP based on the surface engineering, along with their possible sensor applications upon BSA interaction as a proof-of-concept stage. EuIO-Cit showed an r_2 value of 89.1 $mM^{-1}s^{-1}$ and r_1 value of 17.2 $mM^{-1}s^{-1}$ (r_2/r_1 ratio = 5.2). EuIO-PP had an r_2 value of 111.5 $mM^{-1}s^{-1}$ and r_1 value of 1.3 $mM^{-1}s^{-1}$ (r_2/r_1 ratio = 85.8). The r_2 and r_1 values of EuIO-Ale were 231.5 $mM^{-1}s^{-1}$ and 9.9 $mM^{-1}s^{-1}$, respectively (r_2/r_1 ratio = 23.4). Thus, one of key achievements of the current study was that EuIO NPs could act as dual-mode T_1-T_2 or T_2-dominated MRI CAs depending on the surface engineering. Another important achievement was that from BSA interaction results, both the T_1 and T_2 relaxation times changes could provide an "AND logic algorithm" for accurate diagnosis.[10] Our observations on the surface-based relaxivity tuning of DMNP could be expanded to the surface design of stimuli-responsive DMNP. In other words, the relaxivity of DMNP is tunable using surface materials that are responsive to stimuli (such as pH, temperature, redox, enzyme, and light), conferring an MR signal alteration before/after stimulation.[48] In addition, magnetically responsive nanoparticles are applicable as recyclable materials due to the easy recovery.[30, 49] However, additional surface modifications may be required for the specific targeting capture of any pollution and contaminants. Our strategy may open up a new avenue and be a great inspiration for advanced biomedical applications of MRI nanoprobes with T_1-T_2 dual-modality.

ASSOCIATED CONTENT

The Supporting Information is available free of charge on the ACS Publications website at DOI:

The illustration of surface modification, the chemical structures and the reaction scheme of PP; Eu doping level; the M-H curve of EuIO NPs; additional TEM images; DLS measurements; colloidal stability studies; comparison of reported MRI probes and our nanosystems; contact angle measurements; cell viability assay; TGA curves (PDF)

AUTHOR INFORMATION

Corresponding Author

*E-mail: jhseo78@yu.ac.kr
*E-mail: ychang@knu.ac.kr

Notes

The authors declare no competing financial interest.

ACKNOWLEDGMENT

This work was supported by National Research Foundation (NRF) of Korea grants (no. 2017R1C1B1011265) and by a Marine Biomaterials Research Center grant from the Marine Biotechnology Program of the Korea Institute of Marine Science and Technology Promotion, funded by the Ministry of Oceans and Fisheries, Korea. XRD and XPS were performed with the instruments at the Korea Basic Science Institute (KBSI).

REFERENCES

(1) Choi, J. s.; Park, J. C.; Nah, H.; Woo, S.; Oh, J.; Kim, K. M.; Cheon, G. J.; Chang, Y.; Yoo, J.; Cheon, J. A Hybrid Nanoparticle Probe for Dual-Modality Positron Emission Tomography and Magnetic Resonance Imaging. *Angew. Chem. In. Ed.* **2008,** *47*, 6259-6262.

(2) Louie, A. Multimodality Imaging Probes: Design and Challenges. *Chem. Rev.* **2010,** *110*, 3146-3195.
(3) Wu, Q.; Cheng, Q.; Yuan, S.; Qian, J.; Zhong, K.; Qian, Y.; Liu, Y. A Cell-Penetrating Protein Designed for Bimodal Fluorescence and Magnetic Resonance Imaging. *Chem. Sci.* **2015,** *6*, 6607-6613.
(4) Sasaki, M.; Shibata, E.; Kanbara, Y.; Ehara, S. Enhancement Effects and Relaxivities of Gadolinium-DTPA at 1.5 versus 3 Tesla: A Phantom Study. *Magn. Reson. Med. Sci.* **2005,** *4*, 145-149.
(5) Park, J. Y.; Baek, M. J.; Choi, E. S.; Woo, S.; Kim, J. H.; Kim, T. J.; Jung, J. C.; Chae, K. S.; Chang, Y.; Lee, G. H. Paramagnetic Ultrasmall Gadolinium Oxide Nanoparticles as Advanced T $_1$ MRI Contrast Agent: Account for Large Longitudinal Relaxivity, Optimal Particle Diameter, and in Vivo T_1 MR Images. *ACS Nano* **2009,** *3*, 3663-3669.
(6) Lai, W.-F.; Rogach, A. L.; Wong, W.-T. Molecular Design of Upconversion Nanoparticles for Gene Delivery. *Chem. Sci.* **2017,** *8*, 7339-7358.
(7) Tromsdorf, U. I.; Bruns, O. T.; Salmen, S. C.; Beisiegel, U.; Weller, H. A Highly Effective, Nontoxic T_1 MR Contrast Agent Based on Ultrasmall PEGylated Iron Oxide Nanoparticles. *Nano Lett.* **2009,** *9*, 4434-4440.
(8) Kim, B. H.; Lee, N.; Kim, H.; An, K.; Park, Y. I.; Choi, Y.; Shin, K.; Lee, Y.; Kwon, S. G.; Na, H. B. Large-Scale Synthesis of Uniform and Extremely Small-Sized Iron Oxide Nanoparticles for High-Resolution T_1 Magnetic Resonance Imaging Contrast Agents. *J. Am. Chem. Soc.* **2011,** *133*, 12624-12631.
(9) Tong, S.; Hou, S.; Zheng, Z.; Zhou, J.; Bao, G. Coating Optimization of Superparamagnetic Iron Oxide Nanoparticles for High T_2 Relaxivity. *Nano Lett.* **2010,** *10*, 4607-4613.
(10) Shin, T.-H.; Choi, J.-s.; Yun, S.; Kim, I.-S.; Song, H.-T.; Kim, Y.; Park, K. I.; Cheon, J. T_1 and T_2 Dual-Mode MRI Contrast Agent for Enhancing Accuracy by Engineered Nanomaterials. *ACS Nano* **2014,** *8*, 3393-3401.
(11) Lee, N.; Yoo, D.; Ling, D.; Cho, M. H.; Hyeon, T.; Cheon, J. Iron Oxide Based Nanoparticles for Multimodal Imaging and Magnetoresponsive Therapy. *Chem. Rev.* **2015,** *115*, 10637-10689.
(12) Zhou, Z. J. J.; Bai, R. L. L.; Munasinghe, J.; Shen, Z. Y.; Nie, L. M.; Chen, X. Y. T_1-T_2 Dual-Modal Magnetic Resonance Imaging: From Molecular Basis to Contrast Agents. *ACS Nano* **2017,** *11*, 5227-5232.
(13) Yeo, S.; Choi, H.; Kim, C. S.; Lee, G. T.; Seo, J. H.; Cha, H. J.; Park, J. C. Survival of Verwey Transition in Gadolinium-Doped Ultrasmall Magnetite Nanoparticles. *Nanoscale* **2017,** *9*, 13976-13982.
(14) Zhou, Z. J.; Huang, D. T.; Bao, J. F.; Chen, Q. L.; Liu, G.; Chen, Z.; Chen, X. Y.; Gao, J. H. A Synergistically Enhanced T_1-T_2 Dual-Modal Contrast Agent. *Adv. Mater.* **2012,** *24*, 6223-6228.
(15) Yang, L.; Zhou, Z.; Liu, H.; Wu, C.; Zhang, H.; Huang, G.; Ai, H.; Gao, J. Europium-Engineered Iron Oxide Nanocubes with High T_1 and T_2 Contrast Abilities for MRI in Living Subjects. *Nanoscale* **2015,** *7*, 6843-6850.
(16) Zhou, Z. J.; Wang, L. R.; Chi, X. Q.; Bao, J. F.; Yang, L. J.; Zhao, W. X.; Chen, Z.; Wang, X. M.; Chen, X. Y.; Gao, J. H. Engineered Iron-Oxide-Based Nanoparticles as Enhanced T_1 Contrast Agents for Efficient Tumor Imaging. *ACS Nano* **2013,** *7*, 3287-3296.

(17) Huang, G.; Li, H.; Chen, J.; Zhao, Z.; Yang, L.; Chi, X.; Chen, Z.; Wang, X.; Gao, J. Tunable T_1 and T_2 Contrast Abilities of Manganese-Engineered Iron Oxide Nanoparticles through Size Control. *Nanoscale* **2014,** *6*, 10404-10412.
(18) Zhou, Z.; Zhao, Z.; Zhang, H.; Wang, Z.; Chen, X.; Wang, R.; Chen, Z.; Gao, J. Interplay between Longitudinal and Transverse Contrasts in Fe_3O_4 Nanoplates with (111) Exposed Surfaces. *ACS Nano* **2014,** *8*, 7976-7985.
(19) Choi, J.-s.; Kim, S.; Yoo, D.; Shin, T.-H.; Kim, H.; Gomes, M. D.; Kim, S. H.; Pines, A.; Cheon, J. Distance-Dependent Magnetic Resonance Tuning as a Versatile MRI Sensing Platform for Biological Targets. *Nat. Mater.* **2017,** *16*, 537-542.
(20) Qin, J.; Laurent, S.; Jo, Y. S.; Roch, A.; Mikhaylova, M.; Bhujwalla, Z. M.; Muller, R. N.; Muhammed, M. A High-Performance Magnetic Resonance Imaging T_2 Contrast Agent. *Adv. Mater.* **2007,** *19*, 1874-1878.
(21) Zeng, J.; Jing, L.; Hou, Y.; Jiao, M.; Qiao, R.; Jia, Q.; Liu, C.; Fang, F.; Lei, H.; Gao, M. Anchoring Group Effects of Surface Ligands on Magnetic Properties of Fe_3O_4 Nanoparticles: Towards High Performance MRI Contrast Agents. *Adv. Mater.* **2014,** *26*, 2694-2698.
(22) Zheng, X.-Y.; Zhao, K.; Tang, J.; Wang, X.-Y.; Li, L.-D.; Chen, N.-X.; Wang, Y.-J.; Shi, S.; Zhang, X.; Malaisamy, S. Gd-Dots with Strong Ligand–Water Interaction for Ultrasensitive Magnetic Resonance Renography. *ACS Nano* **2017,** *11*, 3642-3650.
(23) Johnson, N. J.; He, S.; Nguyen Huu, V. A.; Almutairi, A. Compact Micellization: A Strategy for Ultrahigh T_1 Magnetic Resonance Contrast with Gadolinium-Based Nanocrystals. *ACS Nano* **2016,** *10*, 8299-8307.
(24) Sun, S.; Zeng, H.; Robinson, D. B.; Raoux, S.; Rice, P. M.; Wang, S. X.; Li, G. Monodisperse MFe_2O_4 (M= Fe, Co, Mn) Nanoparticles. *J. Am. Chem. Soc.* **2004,** *126*, 273-279.
(25) Lattuada, M.; Hatton, T. A. Functionalization of Monodisperse Magnetic Nanoparticles. *Langmuir* **2007,** *23*, 2158-2168.
(26) Yang, H.; Li, X.; Zhou, H.; Zhuang, Y.; Hu, H.; Wu, H.; Yang, S. Monodisperse Water-Soluble Fe–Ni Nanoparticles for Magnetic Resonance Imaging. *J. Alloys Compd.* **2011,** *509*, 1217-1221.
(27) William, W. Y.; Chang, E.; Sayes, C. M.; Drezek, R.; Colvin, V. L. Aqueous Dispersion of Monodisperse Magnetic Iron Oxide Nanocrystals through Phase Transfer. *Nanotechnology* **2006,** *17*, 4483.
(28) Park, J. C.; Lee, G. T.; Seo, J. H. Mannose-Functionalized Core@Shell Nanoparticles and Their Interactions with Bacteria. *J.Mater. Sci.* **2017,** *52*, 1534-1545.
(29) Maleki, A.; Zand, P.; Mohseni, Z.; Firouzi-Haji, R. Green Composite Nanostructure (Fe_3O_4@PEG-SO_3H): Preparation, Characterization and Catalytic Performance in the Efficient Synthesis of β-Amino Carbonyl Compounds at Room Temperature. *Nano-Struct. Nano-Objects* **2018,** *16*, 31-37.
(30) Maleki, A.; Zand, P.; Mohseni, Z. Fe_3O_4@PEG-SO_3H Rod-like Morphology along with the Spherical Nanoparticles: Novel Green Nanocomposite Design, Preparation, Characterization and Catalytic Application. *RSC Adv.* **2016,** *6*, 110928-110934.
(31) Maleki, A.; Movahed, H.; Ravaghi, P. Magnetic Cellulose/Ag as a Novel Eco-Friendly Nanobiocomposite to Catalyze Synthesis of Chromene-Linked Nicotinonitriles. *Carbohyd. Polym.* **2017,** *156*, 259-267.
(32) De Silva, C. R.; Smith, S.; Shim, I.; Pyun, J.; Gutu, T.; Jiao, J.; Zheng, Z. Lanthanide (III)-Doped Magnetite Nanoparticles. *J. Am. Chem. Soc.* **2009,** *131*, 6336-6337.

(33) Song, Q.; Zhang, Z. J. Shape Control and Associated Magnetic Properties of Spinel Cobalt Ferrite Nanocrystals. *J. Am. Chem. Soc.* **2004,** *126*, 6164-6168.
(34) Liang, X.; Wang, X.; Zhuang, J.; Chen, Y.; Wang, D.; Li, Y. Synthesis of Nearly Monodisperse Iron Oxide and Oxyhydroxide Nanocrystals. *Adv. Funct. Mater.* **2006,** *16*, 1805-1813.
(35) Park, J. C.; Yeo, S.; Kim, M.; Lee, G. T.; Seo, J. H. Synthesis and Characterization of Novel Lanthanide-Doped Magnetite@Au Core@Shell Nanoparticles. *Mater. Lett.* **2016,** *181*, 272-277.
(36) Kucheryavy, P.; He, J.; John, V. T.; Maharjan, P.; Spinu, L.; Goloverda, G. Z.; Kolesnichenko, V. L. Superparamagnetic Iron Oxide Nanoparticles with Variable Size and an Iron Oxidation State as Prospective Imaging Agents. *Langmuir* **2013,** *29*, 710-716.
(37) Na, H. B.; Song, I. C.; Hyeon, T. Inorganic Nanoparticles for MRI Contrast Agents. *Adv. Mater.* **2009,** *21*, 2133-2148.
(38) Caravan, P.; Ellison, J. J.; McMurry, T. J.; Lauffer, R. B. Gadolinium (III) Chelates as MRI Contrast Agents: Structure, Dynamics, and Applications. *Chem. Rev.* **1999,** *99*, 2293-2352.
(39) Taylor, K. M.; Kim, J. S.; Rieter, W. J.; An, H.; Lin, W.; Lin, W. Mesoporous Silica Nanospheres as Highly Efficient MRI Contrast Agents. *J. Am. Chem. Soc.* **2008,** *130*, 2154-2155.
(40) Wu, M.; Meng, Q.; Chen, Y.; Xu, P.; Zhang, S.; Li, Y.; Zhang, L.; Wang, M.; Yao, H.; Shi, J. Ultrasmall Confined Iron Oxide Nanoparticle MSNs as a pH-Responsive Theranostic Platform. *Adv. Funct. Mater.* **2014,** *24*, 4273-4283.
(41) Kim, C. R.; Baeck, J. S.; Chang, Y.; Bae, J. E.; Chae, K. S.; Lee, G. H. Ligand-Size Dependent Water Proton Relaxivities in Ultrasmall Gadolinium Oxide Nanoparticles and in Vivo T_1 MR Images in a 1.5 T MR Field. *Phys. Chem. Chem. Phys.* **2014,** *16*, 19866-19873.
(42) Daou, T. J.; Greneche, J. M.; Pourroy, G.; Buathong, S.; Derory, A.; Ulhaq-Bouillet, C.; Donnio, B.; Guillon, D.; Begin-Colin, S. Coupling Agent Effect on Magnetic Properties of Functionalized Magnetite-Based Nanoparticles. *Chem. Mater.* **2008,** *20*, 5869-5875.
(43) Choi, H. S.; Liu, W.; Misra, P.; Tanaka, E.; Zimmer, J. P.; Ipe, B. I.; Bawendi, M. G.; Frangioni, J. V. Renal Clearance of Quantum Dots. *Nat. Biotechnol.* **2007,** *25*, 1165-1170.
(44) Abboud, M.; Youssef, S.; Podlecki, J.; Habchi, R.; Germanos, G.; Foucaran, A. Superparamagnetic Fe_3O_4 Nanoparticles, Synthesis and Surface Modification. *Mater. Sci. Semicond. Process.* **2015,** *39*, 641-648.
(45) Xiong, S.; George, S.; Ji, Z.; Lin, S.; Yu, H.; Damoiseaux, R.; France, B.; Ng, K. W.; Loo, S. C. J. Size of TiO_2 Nanoparticles Influences Their Phototoxicity: An in Vitro Investigation. *Arch. toxicol.* **2013,** *87*, 99-109.
(46) Brewer, S. H.; Glomm, W. R.; Johnson, M. C.; Knag, M. K.; Franzen, S. Probing BSA Binding to Citrate-Coated Gold Nanoparticles and Surfaces. *Langmuir* **2005,** *21*, 9303-9307.
(47) Park, J.-A.; Lee, J.-J.; Kim, I.-S.; Park, B.-H.; Lee, G.-H.; Kim, T.-J.; Ri, H.-C.; Kim, H.-J.; Chang, Y. Magnetic and MR Relaxation Properties of Avidin–Biotin Conjugated Superparamagnetic Nanoparticles. *Colloids Surf. A* **2008,** *313*, 288-291.
(48) Kang, T.; Li, F.; Baik, S.; Shao, W.; Ling, D.; Hyeon, T. Surface Design of Magnetic Nanoparticles for Stimuli-Responsive Cancer Imaging and Therapy. *Biomaterials* **2017,** *136*, 98-114.
(49) Maleki, A.; Movahed, H.; Ravaghi, P.; Kari, T. Facile in Situ Synthesis and Characterization of a Novel PANI/Fe_3O_4/Ag Nanocomposite and Investigation of Catalytic Applications. *RSC Adv.* **2016,** *6*, 98777-98787.

SYNOPSIS.

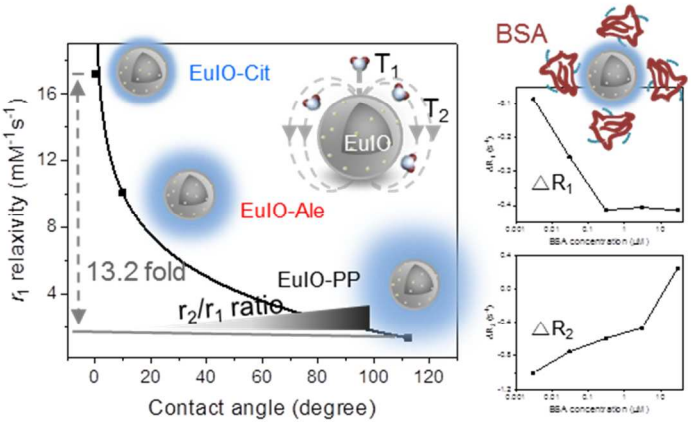
EuIO-Cit
T1
T2
EuIO
EuIO-Ale
EuIO-PP
13.2 fold
r2/r1 ratio
r1 relaxivity (mM-1s-1)
16
12
8
4
0
20
40
60
80
100
120
Contact angle (degree)
BSA
△R1
△R2